# *Foehn jets over the Larsen C ice shelf, Antarctica*

RMetS
Royal Meteorological Society

# Foehn jets over the Larsen C Ice Shelf, Antarctica

Andrew D. Elvidge,[a]* Ian A. Renfrew,[a] John C. King,[b] Andrew Orr,[b] Tom A. Lachlan-Cope,[b] Mark Weeks[c] and Sue L. Gray[d]

[a]*School of Environmental Sciences, University of East Anglia, Norwich, UK*
[b]*British Antarctic Survey, Cambridge, UK*
[c]*Met Office, Exeter, UK*
[d]*Department of Meteorology, University of Reading, UK*

*Correspondence to: A. D. Elvidge, Centre for Ocean and Atmospheric Sciences, School of Environmental Sciences, University of East Anglia, Norwich, NR4 7TJ. UK. E-mail: a.elvidge@uea.ac.uk

**Previously unknown foehn jets have been identified to the east of the Antarctic Peninsula (AP) above the Larsen C Ice Shelf. These jets have major implications for the east coast of the AP, a region of rapid climatic warming and where two large sections of ice shelf have collapsed in recent years.**

**During three foehn events across the AP, leeside warming and drying is seen in new aircraft observations and simulated well by the Met Office Unified Model (MetUM) at ∼1.5 km grid spacing. In case A, weak southwesterly flow and an elevated upwind inversion characterise a highly nonlinear flow regime with upwind flow blocking. In case C strong northwesterly winds characterise a relatively linear case with little upwind flow blocking. Case B resides somewhere between the two in flow regime linearity.**

**The foehn jets – apparent in aircraft observations where available and MetUM simulations of all three cases – are mesoscale features (up to 60 km in width) originating from the mouths of leeside inlets. Through back trajectory analysis they are identified as a type of gap flow. In cases A and B the jets are distinct, being strongly accelerated relative to the background flow, and confined to low levels above the Larsen C Ice Shelf. They resemble the 'shallow foehn' of the Alps. Case C resembles a case of 'deep foehn', with the jets less distinct. The foehn jets are considerably cooler and moister relative to adjacent regions of calmer foehn air. This is due to a dampened foehn effect in the jet regions: in case A the jets have lower upwind source regions, and in the more linear case C there is less diabatic warming and precipitation along jet trajectories due to the reduced orographic uplift across the mountain passes.**

*Key Words:* foehn; Antarctic Peninsula; Larsen Ice Shelf; gap flows; orographic jets; Met Office Unified Model

*Received 30 October 2013; Revised 29 March 2014; Accepted 6 April 2014; Published online in Wiley Online Library 19 June 2014*

## 1. Introduction

The ice shelves surrounding the Antarctic Peninsula (AP) have been in a state of retreat over the past 50 years (Vaughan *et al.*, 2001). On the AP's east coast, for example, the Larsen A and B Ice Shelves collapsed in 1995 and 2002 respectively (Vaughan and Doake, 1996; Rignot *et al.*, 2004). Such events have major implications for regional and global climate, including bringing about sea-level rise via the increased discharge of glacial ice into the ocean (Rignot *et al.*, 2008).

Surface melt due to atmospheric warming is thought to be the main driver of the ice loss (Scambos *et al.*, 2000; van den Broeke, 2005). Indeed, the AP has been one of the fastest warming regions on Earth over the previous 50 years (Vaughan *et al.*, 2003). Moreover, the warming on the east coast is notably greater than that on the west coast during the summer and autumn seasons (Marshall *et al.*, 2006).

Marshall *et al.* (2006) revealed a link between east coast AP warming and the strength of the circumpolar vortex. The circumpolar vortex promotes the westerly transport of warm, moist air from across the Southern Ocean and Bellingshausen Sea to impinge on the Peninsula. If the westerly winds are relatively weak, the low-level eastward transport of these air masses (which are usually stably stratified) is blocked by the AP, especially to the south where the Peninsula is bounded by high mountains (Orr *et al.*, 2008). Under these circumstances, the east side of the AP

is commonly cooler than the west, with cold air of continental origin residing above the Larsen C Ice Shelf, and the AP's west coast being on average 3–5 °C warmer at near-surface level than its east coast at the same latitude (Morris and Vaughan, 2003).

The circumpolar vortex has strengthened in association with a positive shift towards the high-polarity index of the Southern Annular Mode (SAM) since approximately 1965 (Marshall, 2002). Marshall *et al.* (2006) found that summer and autumn temperature variations on the northeast side of the AP were strongly correlated with variations in the SAM index. They suggested that the observed warming to the east of the AP may be due to the stronger and more frequent westerly winds leading to an increase in the volume of air able to pass over the AP from the west, resulting in more frequent downslope 'foehn' winds to the lee of the mountains. This has been called the '*foehn hypothesis*' for east coast AP warming.

The WMO (1992) defines foehn as '*a wind warmed and dried by descent, in general on the lee side of a mountain.*' Although commonly associated with high wind speeds, in this study the term is used to describe any warm, dry downslope flow. The foehn hypothesis is supported in the regional climatology study of van Lipzig *et al.* (2008) and in the model and laboratory experiments of Orr *et al.* (2008). While the existence of individual westerly foehn warming events across the AP has been confirmed in limited aircraft observations (King *et al.*, 2008), and in model simulations with 12 km grid size (Orr *et al.*, 2008), comprehensive observations of foehn flows in this region and higher-resolution numerical modelling studies have not previously been published.

The Orographic Flows and Climate of the Antarctic Peninsula (OFCAP) project was designed to address this shortcoming and investigate various aspects of the foehn hypothesis for the climatic warming on the east coast of the AP. The focus of OFCAP was on the Larsen C Ice Shelf (LCIS; Figure 1(a)). Extending into the Weddell Sea, the LCIS is the largest remaining ice shelf attached to the AP. An intensive field campaign took place between January and February 2011, based at the British Antarctic Survey's Rothera Research Station (Figure 1(a)). Comprehensive aircraft observations were made during several foehn events, both westerly onto the LCIS and easterly.

Here we present the first in-depth analysis of several cases of westerly foehn over the AP. The three cases examined vary greatly in nature according to variable synoptic conditions, allowing our analysis to encompass a broad range of foehn types. Case A (between 4 and 5 February 2011) and case B (27–28 January 2011) were both during the OFCAP field campaign, while case C (15–16 November 2010) is clear in automatic weather station observations from the LCIS (Kuipers Munneke *et al.*, 2012). Here we make use of the first comprehensive aircraft observations of AP foehn flows, as well as high resolution (1.5 km grid size) model simulations and trajectory analysis to characterise and investigate in detail the complex leeside spatial structures found, in particular the propagation of foehn jets above the LCIS. We also investigate the link between strengthening westerlies and near-surface warming and ice melt to the east of the AP. In the next section a brief review of relevant dynamical theory is presented. Section 3 describes the data and methods employed, while section 4 introduces the three cases studied. Sections 5 and 6 detail the characteristics of the foehn events and present the first ever observations of the mesoscale foehn jets discovered to be ubiquitous in this area. Section 7 concludes the article.

## 2. Theoretical context

The basic response of an atmospheric flow encountering a mountain range can be determined via the non-dimensional mountain height, $\hat{h} = Nh/U$, where $N$ is the Brunt–Väisälä frequency of the undisturbed upwind air mass, $h$ is the height of the mountain and $U$ is the wind speed component of the undisturbed upwind flow directed towards and, in the case of an elongated barrier such as the AP, perpendicular to the mountain (e.g. Smith, 1979; Hunt and Snyder, 1980; Trombetti and Tampieri, 1987).

In the case of a continuously stratified atmosphere with little vertical wind shear, for $\hat{h} \ll 1$ solutions obtained from linear theory are qualitatively accurate, describing a flow-over regime for which the disturbance of the mountain on the flow is relatively minor (Durran, 1990). In the case of a stationary orographic gravity wave, linear theory begins to break down as the magnitude of the horizontal wind perturbation $u'$ approaches the background flow speed $U$ somewhere over the barrier (Smith, 1980). Consequently strongly-stratified, slowly-moving flow approaching a high mountain (such that $\hat{h} > 1$) will lead to nonlinear phenomena such as upwind flow blocking, mountain-wave breaking, downslope windstorms and leeside hydraulic jumps (for a comprehensive review of the features of a nonlinear flow regime, see Durran (1990)). Upwind flow blocking describes the separation of upwind flow, whereby air below a certain height (the dividing streamline height, $z_d$) is unable to surmount the mountain and is obstructed, or is forced to flow around rather than over the obstacle (Sheppard, 1956; Smith, 1989).

During foehn events leeside temperatures rise and humidities fall, relative to those upwind of the obstacle. Four mechanisms for leeside warming have been addressed in the literature (e.g. Beran, 1967; Whiteman, 2000; Ólafsson, 2005). The first, termed here *isentropic drawdown*, describes the sourcing of leeside foehn air from higher altitudes upwind of the mountain as a result of upwind flow separation. In a stably stratified atmosphere this air will be potentially warmer and usually drier than the air below. Secondly, orographic uplift may bring about condensation, leading to net warming via *latent heating and precipitation*. Thirdly, *mechanical mixing* with potentially warmer, drier air as the flow passes above the mountains may bring about leeside warming via turbulent sensible heating. Fourthly, *radiative heating* can impart leeside warming via direct radiative heating or sensible heating from the surface.

Although textbook explanations of foehn flows tend to present a two-dimensional picture, in reality irregularities in orography dictate more complex three-dimensional phenomena. Zängl *et al.* (2004) note that Alpine foehn is, with very few exceptions, confined to valleys aligned north–south, originating from mountain passes. This is analogous to gap flows, which form downwind of passes ('gaps') in a mountain ridge. Air accelerates from the gap exit, in association with a decrease in pressure, to form a jet. In relation to the large-scale flow, two archetypal cases of gap flow can be described: those where the gap or valley is aligned parallel to the large-scale flow; and those where the gap or valley is aligned perpendicular to the large-scale flow (Zängl, 2003). In the case of the latter, a cross-mountain geostrophic pressure gradient drives air ageostrophically through the gap, aided by Coriolis turning of the flow towards the mountain due to the effect of surface friction (Overland and Walter, 1981; Zängl, 2002). Gap flows aligned parallel to the flow are also primarily forced by a cross-barrier pressure gradient. In this case the pressure gradient is not forced by synoptic conditions but by upwind flow deceleration due to the blocking effect of the mountains (Zängl, 2002). In addition to the along-gap pressure gradient, the generation of strong winds downwind of a mountain gap can be due to lateral confluence (Pan and Smith, 1999; Gaberšek and Durran, 2004) and mountain-wave-generated vertical momentum flux (Colle and Mass, 1998; Gaberšek and Durran, 2004).

In a blocked regime where the capping height of the blocked air (commonly determined by the presence of an elevated upwind inversion) is *above* the height of gaps in the mountain range, the gaps provide a conduit for the cross-mountain passage of the otherwise blocked air (Flamant *et al.*, 2002). In such cases, the downwind gap jet is usually distinct from the weaker cross-barrier flow above. Such flows have been described in Mayr *et al.* (2007) as *shallow gap flow* and previously as *shallow foehn*. In the case of a linear flow regime, or where blocked air upwind is

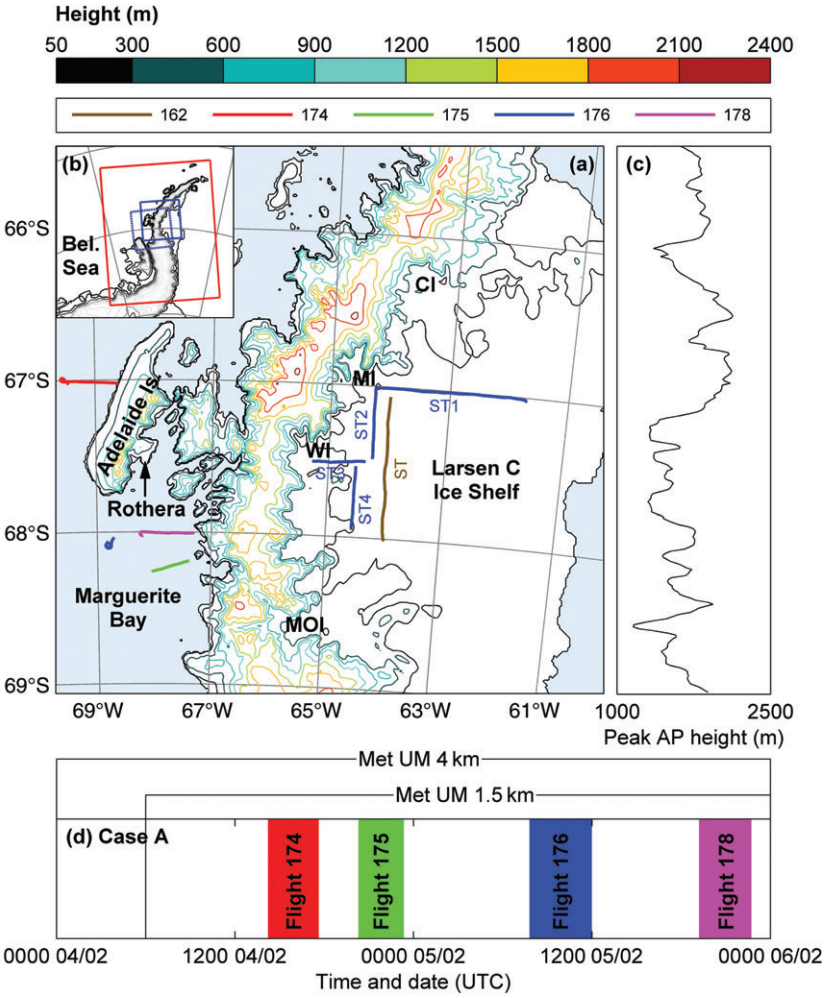


**Figure 1.** (a) Land mask and topographic map from MetUM 1.5 km standard domain orography data (contours, mainly spaced at 300 m) of the section of the AP relevant to this study. Important locations and relevant upwind profile and sawtooth (ST) flight legs are marked, and the sea is shaded pale blue. Note that flights 174, 175, 176 and 178 took place during case A, whilst flight 162 (brown line) took place during case B. MOI = Mobil Oil Inlet, WI = Whirlwind Inlet, MI = Mill Inlet, CI = Cabinet Inlet. (b) Map (inset of (a)) showing the Antarctica Peninsula (and the Bellingshausen Sea to the west), the MetUM 4 km domain (red box), the MetUM 1.5 km standard domain (solid blue box) and the MetUM 1.5 km SW domain (dashed blue box). (c) Peak AP height for each model grid point along the *y*-axis (roughly N–S). Note that passes in the crest line generally coincide with inlets on the eastern slopes of the AP. (d) Timeline showing timing and duration of flights and MetUM simulation periods for case A.

restricted to heights below mountain gaps, the mass flux passing above the higher sections of the barrier is generally large relative to that passing through gaps, resulting in so-called *deep foehn* (Mayr *et al.*, 2007).

## 3. Data and methods

### 3.1. *Description of the study area*

At a maximum height of over 2000 m, length of ∼1500 km and width of ∼200 km, the AP is a significant barrier to atmospheric flow (Figure 1(a,b)). In the vicinity of the LCIS it is a continuous high-level ridge, the crest of which does not fall below 1000 m (Figure 1(c)). However, there are lower sections of the ridge and passes between peaks. Large glacial valleys on the east coast of the AP provide conduits through which downslope flows may be channelled before reaching the LCIS. The deepest of the passes is located upslope of Mobil Oil Inlet (MOI), towards the south of the region of interest (Figure 1(a,c)). North of about 67°S, the ridge bends from being aligned roughly north–south to become aligned roughly northeast–southwest, widens and rises in altitude as the Avery Plateau is encountered. A notable pass is located towards the northern extreme of the region of study, upslope of Cabinet Inlet (CI). Other major inlets include Whirlwind Inlet (WI) and Mill Inlet (MI) (Figure 1(a)).

The presence of the Larsen Ice Shelf to the east of the AP has a major effect on boundary-layer flows (King *et al.*, 2008). The LCIS extends ∼200 km east of the AP, providing a flat, low-friction surface comprising very few orographic or surface complexities. As such, once clear of the orography of the Peninsula, downslope flows are not confined to valleys, as is often the case in, for example, the Alps. Indeed because of this homogeneous leeside surface we would suggest that the AP may be one of the simplest 'natural laboratories' in the world for the study of foehn flows.

### 3.2. *Observations*

Aircraft measurements were made by a De Havilland Canada Twin Otter aircraft, equipped with the Meteorological Airborne Science INstrumentation (MASIN: King *et al.*, 2008; Fiedler *et al.*, 2010). Meteorological variables include wind velocity using a Best Aircraft Turbulence (BAT: Garman *et al.*, 2006) probe, static pressure and total temperature using Rosemount sensors, and humidity using a cooled-mirror hygrometer and a Vaisala Humicap sensor.

Data from four MASIN flights are used to investigate case A (flights 174, 175, 176 and 178; Figure 1(d)), which is the most thoroughly investigated in this study. For case B observations from one flight (MASIN flight 162) document the event. As part of flights 176 and 162, 'sawtooth' legs (ST legs) were flown, i.e. ascending and descending by turn between the near-surface and a predetermined level.

### 3.3. *Modelling*

The Met Office's Unified Model (MetUM: Davies *et al.*, 2005) Version 7.6 has been used for this study, set up similarly to that used in Webster *et al.* (2008) and Orr *et al.* (2014). The MetUM's dynamical core employs a non-hydrostatic, fully compressible, deep atmosphere with a semi-implicit, semi-Lagrangian, predictor–corrector scheme to solve the equations of motion. The MetUM employs Arakawa C-grid staggering in the horizontal and a Charney–Phillips grid in the vertical. The model levels are terrain-following near the surface, but become increasingly level with height (Davies *et al.*, 2005).

A global model with 25 km grid spacing was initialised using the Met Office global operational analysis and run to generate boundary conditions for a limited area model simulation over the AP with a horizontal grid spacing of ∼4 km and 70 vertical levels, 11 of which are within the lowest 500 m above sea level (MetUM 4 km; Figure 1(b)). Within the MetUM 4 km domain, higher-resolution simulations (MetUM 1.5 km) were run, initialised from the 4 km model after 6 h run-time (as illustrated in Figure 1(d) for case A). The MetUM 1.5 km consists of a 270 by 270 horizontal grid, 70 levels in the vertical and a time step of 30 s. Two MetUM 1.5 km domains have been used (both shown in Figure 1(b)), one covering almost the entire LCIS (the 'standard domain') and another, of the same size, located to the southwest (the 'SW domain'). The majority of analysis presented is from the MetUM 1.5 km runs.

The MetUM 4 and 1.5 km models were initialised by relatively high resolution (∼5 km), daily sea ice and sea-surface temperature fields derived from the Operational Sea Surface Temperature and Sea Ice Analysis (OSTIA) system (Stark *et al.*, 2007). The boundary-layer scheme used is as described in Brown *et al.* (2008), and the orographic gravity-wave drag scheme is turned off. The model orography is derived from the Radarsat Antarctic Mapping Project (RAMP) Digital Elevation Model (DEM) of Antarctica (Liu *et al.*, 2001). These high-resolution (200 m grid length) data have been smoothed using a 1-2-1 filter and bilinearly interpolated to the model grid.

## 4. Synoptic situation and upwind conditions

### 4.1. *Case A*

For case A, European Centre for Medium-Range Weather Forecasts ERA-Interim reanalysis (Dee *et al.*, 2011) data show a low-pressure system to the east of the AP, deepening between mid-afternoon on 4 February 2011 and the early morning of 5 February (Figure 2(a)); meanwhile a ridge of high pressure to the west of the AP proceeds east in front of another trough to the west, bringing about a southwesterly cross-barrier flow upwind of the LCIS.

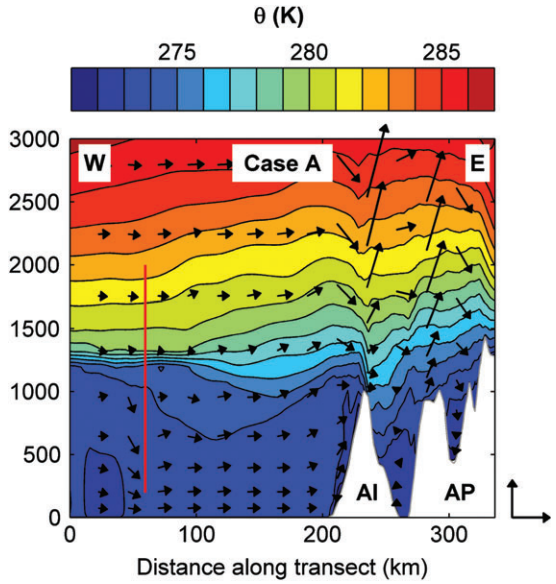


**Figure 3.** Cross-section of potential temperature (contours, spaced at 1 K) and along-transect wind vectors at 0200 UTC on 5 February 2011 during case A along the west–east transect marked in Figure 2(a). The red vertical line marks the sounding position (∼150 km west of Adelaide Island, AI) and depth over which upwind model diagnostics presented in Table 1 correspond to. Orography is in white. For scale, the vectors to the right of the plot correspond to 20 m $s^{-1}$ in the horizontal and 0.2 m $s^{-1}$ in the vertical. Vertical to horizontal scale of axes = 1:100.

Table 1 shows values of MetUM 4 km simulated wind speed, wind direction and $\hat{h}$ representative of each case. These values are calculated for a location $\lambda_R \approx 150$ km west of the AP (location marked on Figure 2), vertically averaged (between 200 and 2000 m; considered to be representative of the flow impinging on the AP) and time-averaged over 2 h periods (deemed to be representative of upwind conditions for each event). Here, $\lambda_R = Nh/f$ (where $f$ is the Coriolis parameter) is the Rossby radius of deformation – upwind of this location the flow does not 'feel' the mountains. For case A, $\hat{h}$ is calculated using the westerly component of the flow (5.9 m $s^{-1}$), i.e. that which is roughly perpendicular to the AP south of ∼ 67°S, with westerly $\hat{h}$ of 3.4 indicating a relatively nonlinear flow regime, for which partial upwind flow blocking is to be expected.

Figure 3 shows the vertical range over which the upwind diagnostics are calculated (red line) against a cross-section of MetUM 4 km simulated potential temperature ($\theta$) and wind vectors along a transect (marked on Figure 2) extending roughly

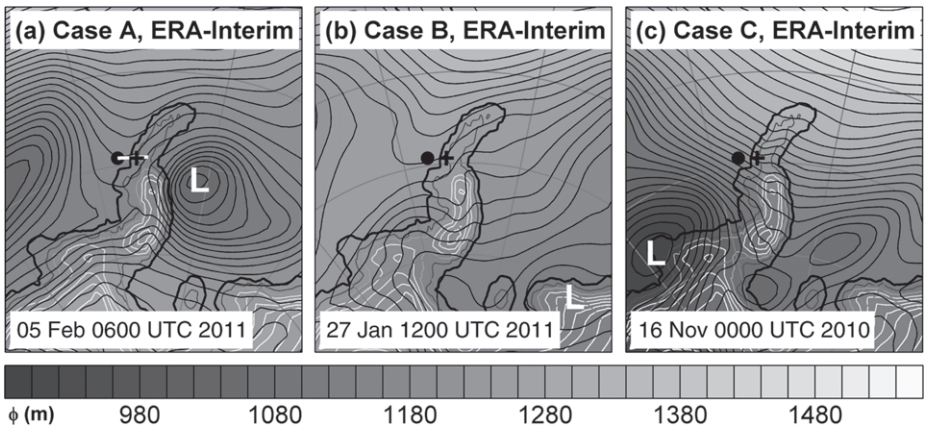


**Figure 2.** Geopotential height (contours, spaced at 15 m) at the 850 hPa level, from ECMWF ERA-Interim reanalysis during each of the cases: (a) case A, (b) case B, and (c) case C. The black dot marks the location 150 km west (∼upwind) of the AP that the upwind model diagnostics presented in Table 1 correspond to. The white line in (a) is the transect line used in Figure 3. The cross marks the position of Rothera Research Station.

Table 1. Diagnostics of undisturbed upwind flow, derived from MetUM 4 km data.

| | Case A | Case B | Case C |
|---|---|---|---|
| Wind speed (m $s^{-1}$) | 6.7 | 4.1 | 22.8 |
| Wind direction (degree (°) from north) | 241 | 267 | 298 |
| $N$ ($\times 10^{-2}$ $s^{-1}$) | 1.33 | 1.11 | 1.17 |
| $\hat{h}$ | 3.4 | 4.1 | 0.9 |

200 km upwind of Adelaide Island, at 0100 UTC on 5 February (upwind diagnostics presented in Table 1 were calculated between 0000 and 0200 UTC). Flow with a westerly component is shown to be approaching the AP throughout the depth of the cross-section (Figure 3). There is little vertical wind shear apart from a slight strengthening towards the top of the cross-section. Westerly winds over the mountains show that at least some of the approaching flow passes over the AP. Note that this cross-section is largely representative of flow across the Peninsula upwind of the Larsen C south of about 67°S (i.e. south of the AP's 'bend'; Figure 1).

An important feature of the flow is an elevated inversion upwind of the AP. This is evident during the flight 176 upwind profile leg within Marguerite Bay at ∼1250 m (Figure 4(a)). It is also captured in the model at a similar height (evident for example in Figure 3). Elevated inversions have been shown to have a significant influence on the ensuing flow regime, particularly in encouraging nonlinear flow characteristics (Brinkmann, 1974; Durran, 1986) and gap flows (Flamant *et al.*, 2002; Mayr *et al.*, 2007). This inversion, capping a relatively cool reservoir of air and positioned well below the height of the AP's higher sections but roughly level with its lower sections (the gaps; Figure 1(c)), indicates the potential for *shallow gap flows* sourced from the cool air reservoir.

In comparisons with aircraft data the MetUM 1.5 and 4 km simulations are shown to perform very well in their reproduction of upwind flow speed and direction, and adequately in their reproduction of upwind static stability (appendix S1).

### 4.2. Case B

For case B, ERA-Interim reanalysis shows relatively low pressure to the east and a ridge to the west of the AP bringing southwesterly flow to the Peninsula on 26 January 2011. As the ridge migrates eastward and the relatively weak low-pressure system moves south, flow becomes more westerly with a stronger cross-Peninsula component in the vicinity of the LCIS (illustrated via the pressure gradient apparent in Figure 2(b)). Upwind conditions are less statically stable than in case A; although, due to weaker winds (a westerly component of 4.1 m $s^{-1}$) the westerly $\hat{h}$ is a little larger at 4.1 (Table 1). Despite this, there is no elevated upwind inversion in case B, and the resulting flow regime is more linear than in case A. Vertically averaged upwind aircraft observations from a single flight during this case compare favourably with equivalent MetUM 4 km values (Table S1).

### 4.3. Case C

Whereas cases A and B were relatively transient westerly flow events, case C covers the final few days of a prolonged episode (several weeks) of cross-Peninsula flow which was associated with a shrinking of the circumpolar vortex and, specifically in the vicinity of the AP, the presence of persistent high pressure north of the AP. This resulted in an enhancement of the meridional pressure gradient and hence the mean westerly component of flow at higher latitudes. This is illustrated for the period of focus in Figure 2(c): on 16 November 2010, a deep low-pressure system is centred south of 68°S and to the west of the Peninsula, bringing northwesterly flow across the AP. Winds simulated upwind of the AP are northwesterly for the most part and considerably stronger than in the other cases (Table 1). The $\hat{h}$ in this case is calculated using the northwesterly component of flow (20 m $s^{-1}$), i.e. that which is roughly perpendicular to the AP north of ∼67°S. Northwesterly $\hat{h}$ of 0.9 indicates a relatively linear, flow-over regime. Upwind vertical cross-sections (not shown) reveal little vertical wind shear above the boundary layer and little vertical variation in $N$ except for a weak elevated inversion at ∼500 m (considerably weaker and at a lower height than that in case A).

## 5. Foehn characteristics

### 5.1. Cases A and B

Analysis of aircraft data from successive flights above the LCIS during case A reveals warming and drying associated with the incursion of westerly winds typical of a westerly foehn event. For example, Figure 4 shows upwind and downwind profiles of $\theta$ and specific humidity ($q$) from aircraft observations for pre-foehn (flight 174) and mid-foehn (flight 176) conditions. A warming and drying of leeside air beneath ∼1200 m is evident between the two flights. Note that this is despite flight 174 taking place during the day and flight 176 being at night/early morning. During flight 174 upwind conditions are warmer and drier than downwind conditions (except below ∼550 m, for which humidities are similar). By flight 176 this situation has reversed, the warmer, drier leeside air being characteristic of foehn conditions in the immediate lee of the AP. In addition to the temperature and humidity gradient, a cross-AP pressure gradient is present in the

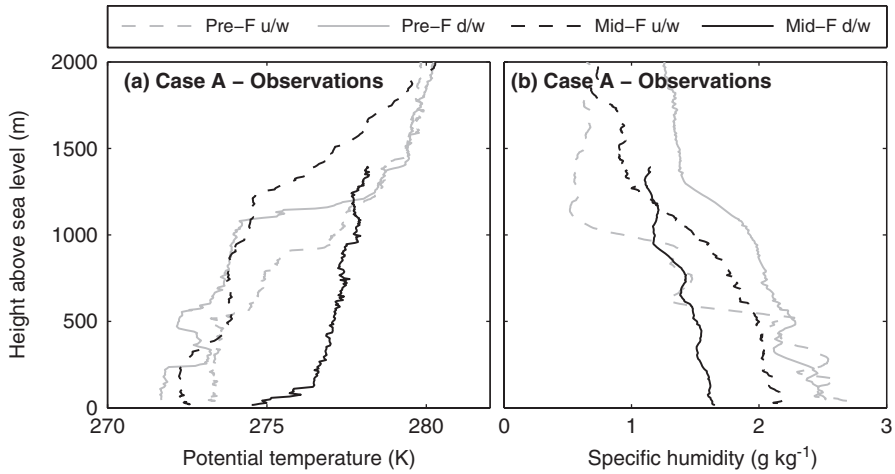


**Figure 4.** Profiles of (a) $\theta$ and (b) $q$ derived from upwind (u/w) and downwind (d/w) components of flight 174 (pre-foehn, in grey) and flight 176 (mid-foehn, in black). The locations of the upwind profiles are marked on Figure 1(a), whilst downwind profiles are within Mill Inlet (MI in Figure 1(a)).

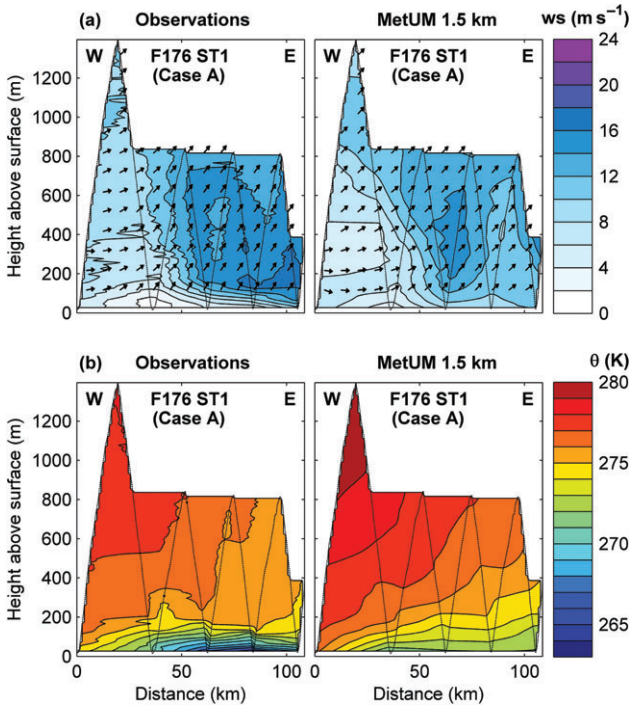


**Figure 5.** Cross-sections of (a) wind speed (contours, spaced at 2 m $s^{-1}$) and wind direction (arrows; the bearing of which denotes the horizontal direction of flow) and (b) $\theta$ (contours, spaced at 1 K) for flight 176 ST1 during case A on the morning of 5 February 2011. Left shows the aircraft observations; right shows MetUM 1.5 km output (interpolated in four dimensions to the flight track). The cross-section is approximately west–east (see Figure 1(a)) with distance marked from the most westerly point. The dotted line denotes the flight path.

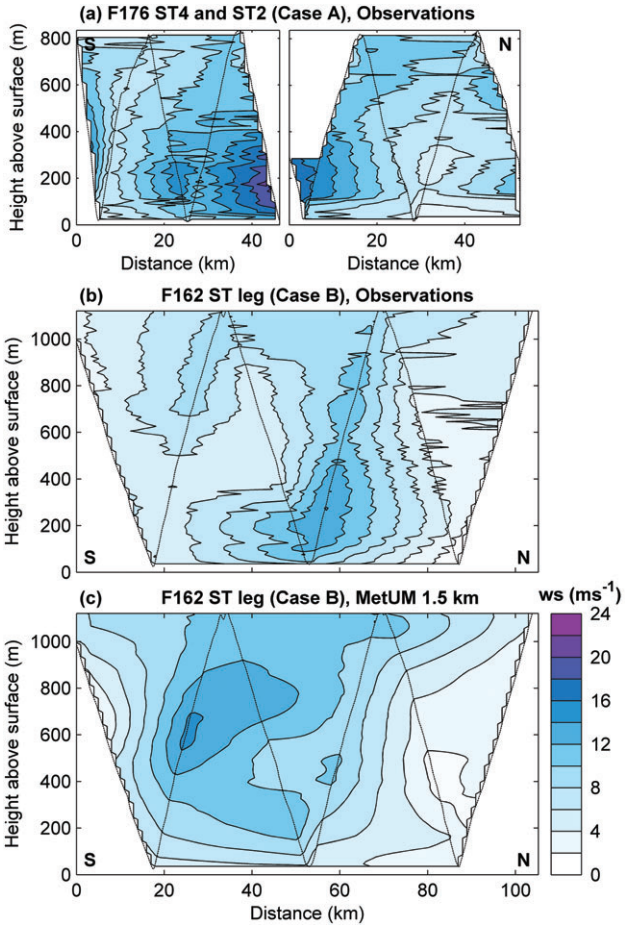


**Figure 6.** Cross-sections of westerly wind speed (contours, spaced at 2 m $s^{-1}$) for (a) flight 176 ST4 (left) and ST2 (right) during case A on the morning of 5 February 2011 from observations and (b, c) the flight 162 ST leg during case B on the afternoon of 27 January 2011 from (b) observations and (c) the MetUM 1.5 km simulation. The cross-sections are approximately south–north, across the foehn jets, with distance from the most southerly point.

MetUM 1.5 km simulation (not shown), the descending leeside air being associated with a low pressure anomaly (a typical feature of cross-barrier flow: Smith, 1979).

The foehn effect is also evident during case A in cross-sections of wind velocity and $\theta$ interpolated horizontally from data derived from flight 176 ST leg 1 (ST1), during which the aircraft flew westward above the LCIS along 67°S (see Figure 1(a) for all flight tracks) roughly midway through the foehn event on the early morning of 5 February 2011 (Figure 5). The encroachment of the warm foehn air from the west is apparent, with relatively high temperatures close to the base of the AP's lee slopes at the western extent of the flight leg. Moving east along the flight leg, near-surface temperatures decrease rapidly and the boundary layer becomes considerably more stable. Such a nocturnal near-surface inversion is a common feature above the ice shelf. The contrast between the warm anomaly induced by the foehn effect close to the AP and the stable cold pool leads to a horizontal gradient in near-surface temperature of ∼10 K over 60 km. Above the surface inversion across the eastern extent of the transect, winds are considerably stronger than closer to the Peninsula, and are southwesterly as opposed to westerly. A second companion article (Elvidge *et al.*, 2014) investigates the distribution of leeside warming in more detail.

Equivalent cross-sections derived from MetUM 1.5 km data (interpolated in four dimensions to the flight track) generally compare well, capturing the westerly to southwesterly flow transition and the warming from the west (Figure 5). However, the model fails to capture the magnitude of the nocturnal inversion (the discrepancy in near-surface temperature peaking at ∼6 K, towards the eastern extent of the flight leg). The model captures the southwesterly flow above the inversion but wind speeds are generally underestimated here.

Figure 6(a) shows north–south cross-sections of westerly wind speed interpolated horizontally from data derived from the flight 176 ST2 and ST4 legs during case A. The two legs are not continuous, the more southerly leg commencing ∼13 km to the west and ∼30 min later than the termination of the more northerly leg. Nevertheless, a low-level jet is evident with peak wind speeds of ∼20 m $s^{-1}$ at ∼200 m above mean sea level (AMSL) roughly intersecting (in the meridional sense) the two legs. The magnitude and position of the jet is captured to a good degree of accuracy in the ST2 profiles simulated by the MetUM 1.5 km; however, a well-defined jet is not apparent in the simulated ST4 leg (equivalent model plots not shown).

A 'cleaner' illustration (due to the continuity of data) of a similar jet in a similar location is provided by case B observations from the north–south flight 162 ST leg (Figure 6(b)). This jet is weaker (wind speeds peaking at ∼14 m $s^{-1}$) than in case A. Peak wind speeds are again observed at relatively low levels (below 400 m) above the ice shelf. The MetUM 1.5 km captures the structure and magnitude of this jet reasonably well (Figure 6(c)), though with peak wind speeds occurring at a slightly higher altitude (∼600 m) and further south (some model discrepancy is to be expected given the non-stationary gusty nature of the foehn jets).

During case A, in the intervening time between the flight 176 ST2 and ST4 legs, the aircraft made a westward diversion to fly upwind within the jet into the mouth of Whirlwind Inlet (ST3; Figure 1(a)). Figure 7 shows cross-sections from ST3 and reveals a correspondence between wind speed and $\theta$ above ∼200 m. Air within the stronger sections of the jet is cooler than that in the weaker flow (to the top and east of the profile). A weaker correspondence exists between wind speed and $q$, with regions of stronger winds appearing to exhibit lower humidities.

In case A, a stable, moist layer was observed immediately above the ice shelf. As illustrated in Figure 7(a) and verified by

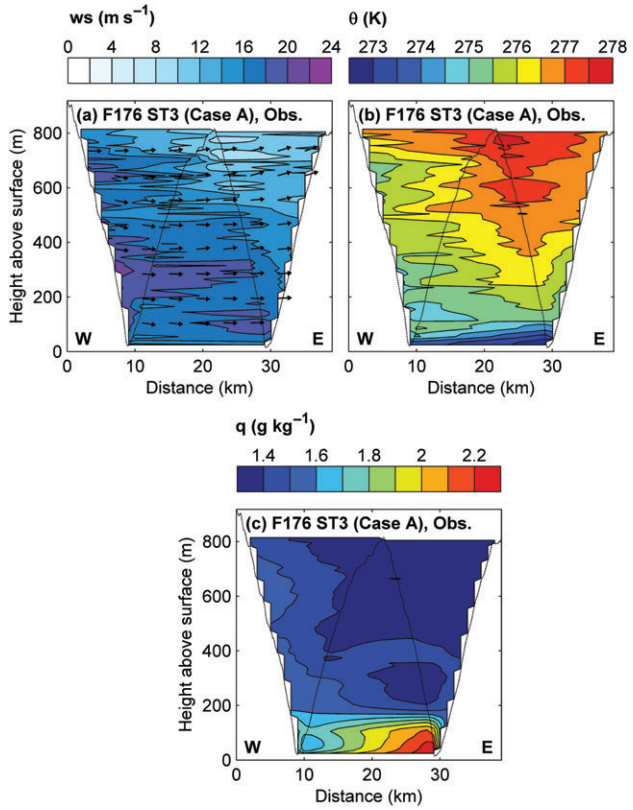


**Figure 7.** Cross-sections of (a) wind speed (contours, spaced at 2 m $s^{-1}$) and wind direction (arrows), (b) $\theta$ (contours, spaced at 0.5 K) and (c) $q$ (contours, spaced at 0.1 g $kg^{-1}$) for flight 176 ST3 during case A on the morning of 5 February 2011. The cross-section is approximately west–east, within the foehn jet.

observations of windblown snow above the ice and of sastrugi (ridged patterns of snow formed by wind erosion) on the ice surface (orientated such as to indicate formation by westerly windblown snow), strong westerly winds extended to near-surface level. This suggests the surface inversion here is not due to the remnants of a cool pool. Instead, loss of sensible heat to the ice surface and gain in moisture due to enhanced sublimation rates driven by the strong surface winds appear to be responsible for the moist stable layer (this interpretation is also supported by model analysis not presented here).

Observations during case A show that the foehn air had penetrated to the near-surface above the LCIS close to the eastern slopes of the AP by the early morning of 5 February (Figure 5). Figure 8 illustrates conditions at 1000 UTC on 5 February (during mid-foehn flight 176) as simulated by the MetUM 1.5 km. Figure 8(a–c) are horizontal 'plan' plots at 150 m AMSL of wind velocity, temperature and $q$ respectively. Figure 8(b,c) illustrate the effect of the westerly foehn; conditions above the LCIS are predominantly warmer and drier than those to the west of the Peninsula. In agreement with observations, leeside temperatures are considerably higher close to the Peninsula's slopes than they are further east. The flow field is inhomogeneous, characterised by jets emanating from the mouths of inlets separated by regions of calmer or stagnant flow (referred to as 'wakes' here). Although the strongest wind speeds are simulated within the inlets, the jets are apparent far downwind of the AP over the LCIS. We surmise that the far-reaching propagation of the jets is largely due to low friction over the smooth ice surface and the statically stable boundary-layer conditions which will suppress mixing.

The jet observed during case A within and downwind of Whirlwind Inlet (Figures 6 and 7) is clearly reproduced by the model (Figure 8(a)). Wind direction close to the Peninsula's eastern slopes appears largely to be a function of the orientation of the inlets through which the outflows are funnelled. Major jets include those emanating from Whirlwind Inlet, Mobil Oil Inlet and Cabinet Inlet. Cross-sections of along-jet wind, $\theta$ and $q$ across each of these jets are also presented in Figure 8(d–f). The simulated jets are distinct and exhibit peak wind speeds at low levels (between about 150 and 400 m), as was observed for the WI jet (though at a location further downwind; Figure 6(a)). The broadest jet is that within MOI, though all three named jets are between 20 and 30 km across close to the base of the lee slopes.

Away from the Peninsula on the leeside, the flow is largely southwesterly. Examination of Figure 8(a) affords understanding as to the flow variability observed and simulated along 67°S for flight 176 ST1 (Figure 5(a)). According to the model, the weak westerlies towards the western end of the ST leg are associated with the relatively weak outflow emanating from MI (see Figure 1(a) for location). On the other hand, the stronger inversion-capping southwesterlies to the east are sourced from the stronger foehn jets to the south.

The jet transect plots of Figure 8 show that, close to the mouth of the inlets, the jets are *cooler and moister relative to the adjacent wakes* (by 3–4 K and 0.5–0.7 g $kg^{-1}$), consistent with the aircraft observations (e.g. Figure 7). The exception is the Mobil Oil Inlet jet, which is dry relative to the wake region to the south (Figure 8(f)). It is important to note that, whilst generally cooler and moister than the wake regions in the immediate lee of the AP, the air advected onto the LCIS within the jets is still warm relative to air west of the AP at the same altitude, and the air further east above the ice sheet.

Similar model plots for case B (not shown) resemble those for case A; the foehn effect is evident in warmer and drier conditions on the leeside (though the amplitude of this foehn anomaly is smaller), with westerly leeside jets being generally weaker but again exhibiting cool, moist signatures relative to neighbouring wakes.

### 5.2. *Case C*

As described in section 4, case C is a more linear foehn event than cases A and B (i.e. $\hat{h} < 1$). The strong northwesterly winds are associated with a foehn effect apparent in higher temperatures and lower humidities downwind than upwind of the AP (Figure 9). Foehn jets are again apparent, plan plots of flow velocity, temperature and $q$ (Figure 9(a–c)) showing clearly their cool, moist nature relative to adjacent regions of calmer flow ('wakes'), by 3–4 K and up to 1.2 g $kg^{-1}$. This is also illustrated in Figure 9(d–f), which shows wind speed, $\theta$ and $q$ for a single transect across the WI, MI and CI jets. Note that although the jets are stronger than in case A (reaching speeds in excess of 30 m $s^{-1}$), they are generally less distinct owing to the stronger background foehn flow, and at a higher level – generally between 400 and 800 m – than case A. Though their indistinct nature renders it difficult to assess their width, one can determine the jets are broader than in case A (the CI jet is ~60 km wide close to the AP). As a result of the linearity of the event, the jets maintain their structure further downwind than in case A (investigated further in Elvidge *et al.* (2014)). This is associated with more widespread low-level foehn warming in case C, extending all the way across the LCIS (Figure 9).

## 6. Foehn trajectories

The cool, moist nature of the foehn jets relative to adjacent wakes in all three cases suggests a difference in source region and/or in cross-Peninsula diabatic heat exchange for the constituent air. Following a review of observational and model studies on gap winds in association with downslope winds and foehn flow, we hypothesise that these jets are the downwind continuation of gap flows through passes across the AP. To test this hypothesis, to investigate why the foehn jets have a cool, moist signature, and to examine differences in the nature of the jets, the trajectory model Lagranto (Wernli and Davies, 1997) is employed to provide a

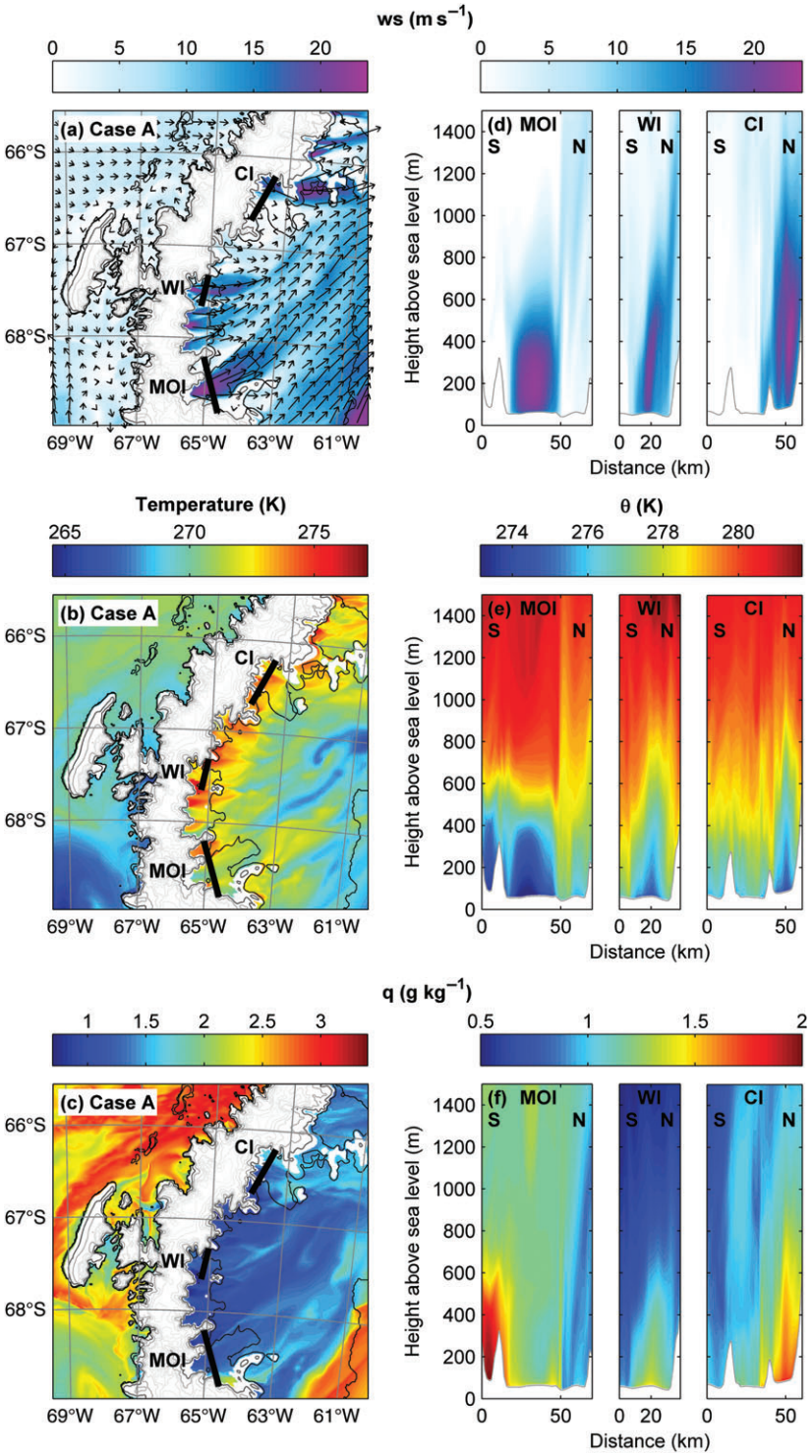


**Figure 8.** Plan ($x - y$) plots at 150 m AMSL of (a) wind speed and vectors, (b) temperature and (c) $q$, and jet cross-sections of (d) transect-normal wind component, (e) $\theta$ and (f) $q$ across Mobil Oil Inlet (MOI), Whirlwind Inlet (WI), and Cabinet Inlet (CI) at 1000 UTC on 5 February 2011 (the time of back trajectory initiation) during case A from the MetUM 1.5 km simulation. Note that in (d) the normal wind component is shown, while for reasons of clarity the small negative wind components (which never exceed a magnitude of 5 m s$^{-1}$) are not shown. Note the colour scales are different for plan and transect plots (except for wind speed). Transect lines are marked on the plan plots. Vertical to horizontal scale of transect plot axes = 1:100.

Lagrangian analysis of the cross-Peninsula flow. MetUM 1.5 km data are used as input for the calculation of back trajectories initiated at every grid point within assigned regions to the east (leeside) of the AP. Lagranto is run backwards in time for a period of up to 24 h (more than sufficient considering the size of the MetUM 1.5 km domain) and with a time resolution of 3 min (such a small time step was used to complement the high spatial resolution of the MetUM 1.5 km simulations). The Lagrangian evolution of physical variables along these paths is then evaluated.

Four diagnostics are examined: the maximum height of the underlying orography traversed; the height of the air parcels (as they cross the Peninsula and at predefined along-transect distance increments upwind); and the air parcel's $\theta$ and $q$.

The back trajectories are initiated within six predefined regions (all marked in Figure 10). Each region is either associated with strong winds, i.e. *jet conditions* (trajectories with initial flow speed $>15$ m s$^{-1}$); or weak winds, i.e. *wake conditions* (trajectories with initial flow speed $<5$ m s$^{-1}$). Exceptionally, some small isolated patches of stronger flow ($>5$ m s$^{-1}$) within the wakes are included within the respective sample regions for technical simplicity. The regions are summarised in Table 2.

In addition to the model domain used in the analyses presented thus far (the standard domain), a second domain for the MetUM

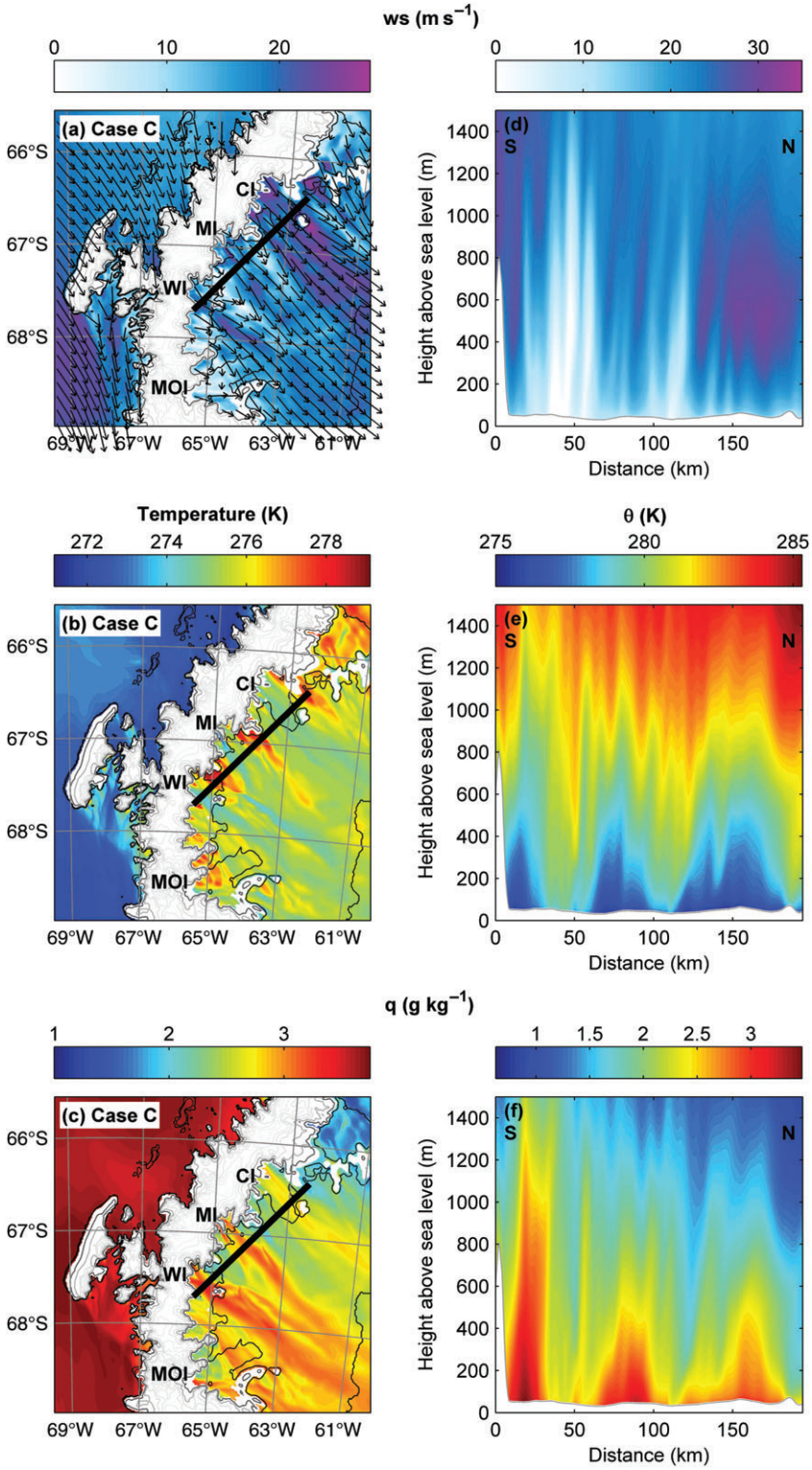


**Figure 9.** Plan and cross-section plots of (a) wind speed, (b) temperature and (c) $q$, as in Figure 8 but for case C at 2200 UTC on 15 February 2011 (the time of back trajectory initiation). The cross-sections (d–f) are along a transect passing through the three major foehn jets during case C; WI, MI and CI.

1.5 km model positioned to the southwest (SW domain; see Figure 1(b)) is used where necessary (for the four southernmost trajectory initiation regions in case A) to avoid the premature departure of trajectories from the model grid. This is for the benefit of cross-case comparison, allowing that for one pair of jet and wake regions (WI and north (N) of WI) trajectories extend beyond the 150 km increment for all three cases (a condition met in cases B and C using the standard domain alone, but not in case A). Despite the fact the change in domain entails an entirely different simulation, both simulations are forced by the same MetUM 4 km simulation and the reproduction of the major features discussed thus far is very similar, with comparable jets and wakes simulated in the immediate lee of the Peninsula (e.g. see Figure 10).

### 6.1. *Case A*

For case A, the trajectories are initiated at 1000 UTC on 5 February (coincident with aircraft observations during flight 176 and Figure 8) from near the base of the lee slope (at 950 hPa; ∼250 m AMSL in this case), and run backwards in time for 24 h. Figure 10 shows trajectories in the horizontal initiated within the WI and CI jet regions. Upwind of the AP the trajectories are generally tightly clustered in horizontal space (a feature common

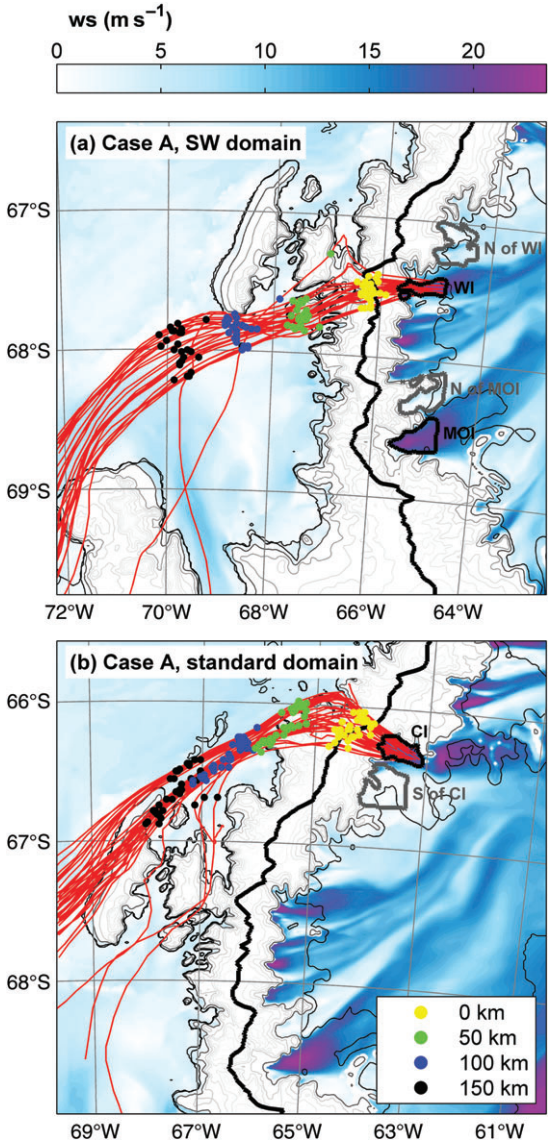


**Figure 10.** Case A back trajectories (red) initiated within (a) the WI jet region in the SW domain and (b) the CI jet region in the standard domain, overlaying wind speed at the 950 hPa level at the time of trajectory initiation (1000 UTC 5 February 2011). To enhance legibility only one in four trajectories is plotted. The yellow, green, blue and black dots indicate the positions of air parcels respectively 0, 50, 100 and 150 km upwind of the AP's crest line (solid black line) for each trajectory. The six trajectory initiation regions are marked and labelled; black boundaries enclose 'jet' regions, whilst grey boundaries enclose 'wake' regions.

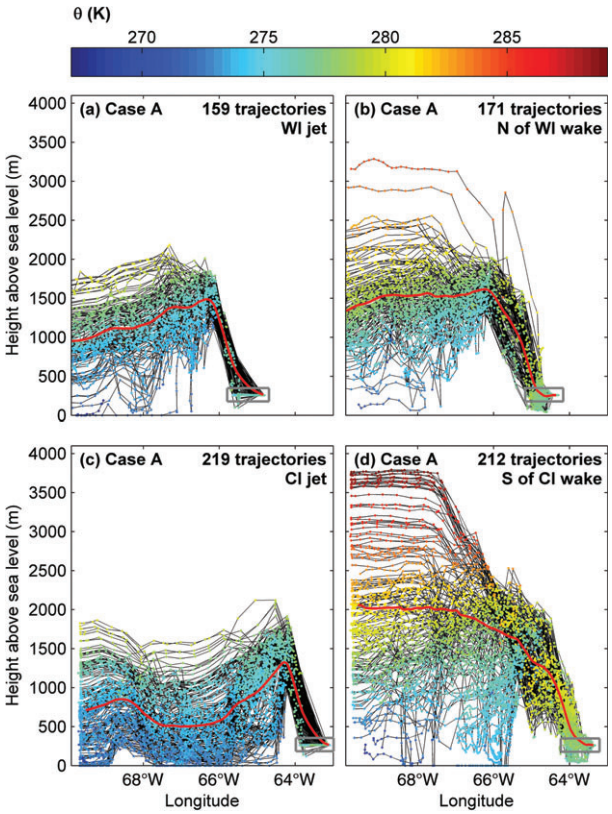


**Figure 11.** Trajectory height vs. longitude for case A. Dots mark the height of air parcels at each point (spaced 30 min apart), with the colour denoting $\theta$ (K) of the air parcel. Trajectory initiation regions are marked by the grey rectangles. Trajectories are initiated within (a) the WI jet, (b) the N of WI wake, (c) the CI jet and (d) the S of CI wake. The thick red lines give the mean trajectory height. In (a) and (c), all trajectories are plotted, whereas in (b) and (d), due to the larger size of the regions, only half the trajectories are plotted to improve legibility.

Table 2. Details of the trajectory initiation regions.

| Full region name | Abbreviation | Type | Domain used for case A |
|---|---|---|---|
| Whirlwind Inlet | WI | Jet | SW |
| North of Whirlwind Inlet | N of WI | Wake | SW |
| Mobil Oil Inlet | MOI | Jet | SW |
| North of Mobil Oil Inlet | N of MOI | Wake | SW |
| Cabinet Inlet | CI | Jet | Standard |
| South of Cabinet Inlet | S of CI | Wake | Standard |

to the MOI jet region and, to almost the same degree, the wake regions – not shown), implying the foehn jets are well-defined features and may have a common forcing mechanism. Figure 11 shows longitude–height plots of the back trajectories from four regions, with the coloured dots indicating $\theta$ along the Lagrangian paths. It is clear that the trajectories are generally lower and colder on the upwind side of the jets, than the wakes. However, within each region there is considerable variation in the upwind source altitude, particularly for the wakes. In the case of the CI jet the major bulk of air is derived from altitudes lower than the AP's crest (see Figure 1(c)); indeed a significant quantity of air is simulated to have risen from near-surface level. A far greater proportion of air has been drawn down from high altitudes in the south (S) of CI wake, and comparatively little air is derived from low levels. The same differences are discernible (though considerably smaller) when comparing the WI jet and N of WI wake trajectories. Note that a greater proportion of the air within the jets is sourced from altitudes below 1250 m – roughly the height of the elevated upwind inversion (Figure 3).

Note in Figure 11(c) there is a 'bump' in the trajectories west of 68°W as they rise over Adelaide Island (see Figure 10(b)). However, the amplitude of this orographic disturbance to the flow is quite small relative to the differences in source altitude between the CI jet and S of CI wake regions (Figure 11(c,d)).

Figure 12 summarises the trajectory analysis, showing the numbers of trajectories and the averages of height, $\theta$, equivalent potential temperature ($\theta_e$) and $q$ versus distance upwind (note that these distances are approximate as for each individual trajectory they relate to the time step for which the along-trajectory length upwind of the AP is closest to the distance). Note that $\theta_e$ here is calculated so as to be conserved for latent heat exchange not only due to condensation and evaporation (as in Bolton, 1980) but also due to freezing and melting. The latter processes are important in our case-studies, due to high cloud ice contents – virtually all precipitation above the AP falls as snow rather than rain. For all jet/wake pairs, both the mean height of the orography traversed and mean upwind trajectory altitudes are greatest for trajectories originating in wake regions (Figure 12). The values reveal consistently large differences in the source altitude between the jet and wake regions, and indicate that the jets appear downwind of flow through passes in the orography (this is also apparent in Figure 1(a,c); passes/depressions in the crest line generally coincide with the positions of inlets on the eastern slopes of the AP). In other words, they are, as hypothesised, *gap winds*. The CI jet and S of CI wake regions exhibit the greatest

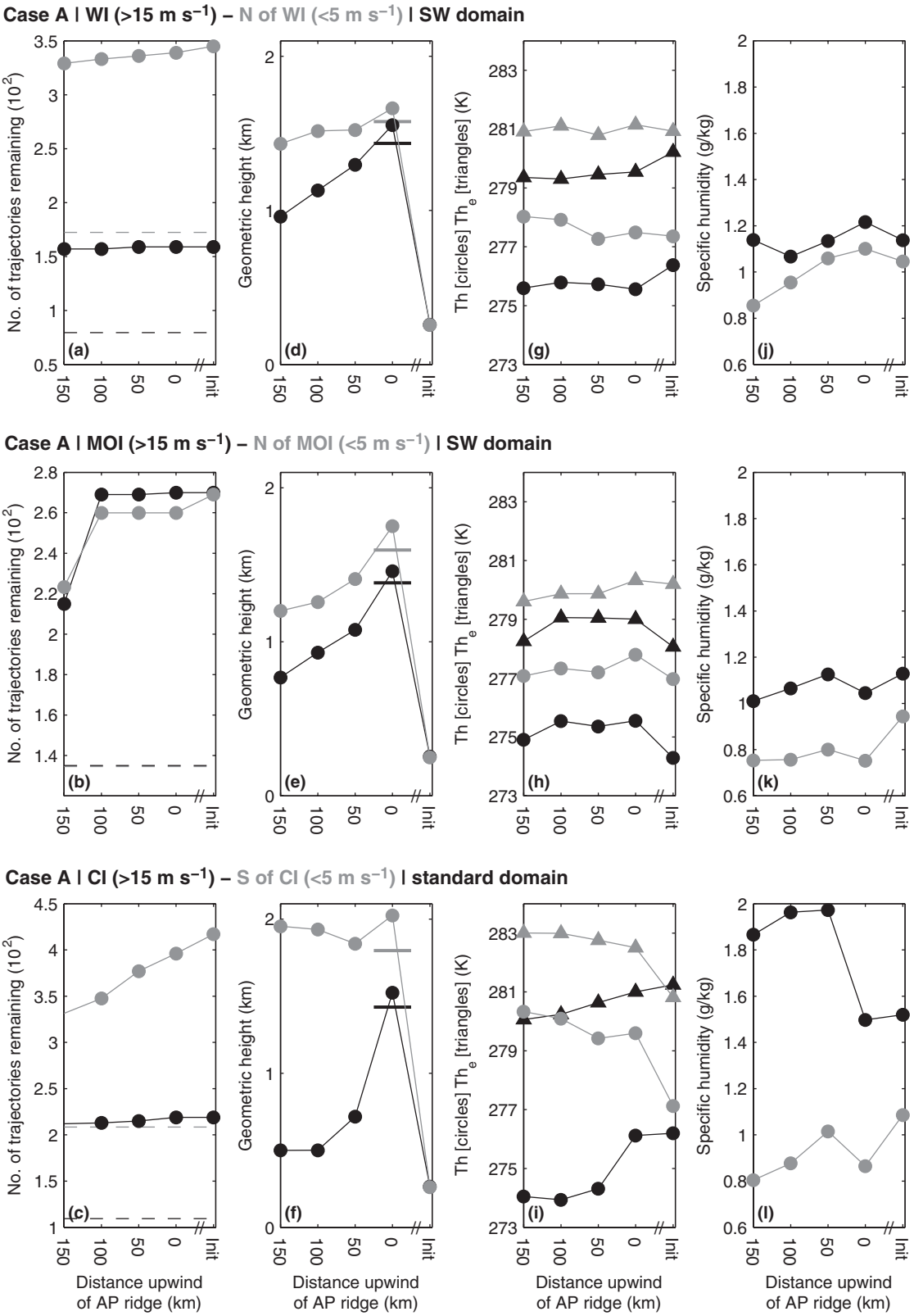


**Figure 12.** Lagrangian changes following back trajectories initiated at 1000 UTC 5 February 2011 during case A within each of the jet (black lines) and wake (grey lines) regions. The five diagnostics illustrated are (a-c) number of trajectories; (d-f) geometric height; (g-i) $\theta$ (Th; circular markers) and equivalent $\theta$ ($Th_e$; triangular markers); and (j-l) $q$. The $x$-axis is trajectory distance upwind of the AP, but also includes an increment for trajectory initiation ('Init') above the Larsen. The dashed horizontal lines in the left panels correspond to half the total number of trajectories. The horizontal lines in the trajectory height panels are the mean estimated peak heights of orography traversed for each set of trajectories.

jet–wake difference in mean trajectory source altitude, around 1500 m, as compared to between 400 and 500 m for the other two jet–wake pairs. As described in section 5.1, the gap jets downwind of the AP during case A are distinct – contrasting with the weaker cross-Peninsula flow aloft – and are restricted to low levels (Figures 6(a) and 8(d)). As such they may be described as *shallow gap flows*, or *shallow foehn* (e.g. Mayr *et al.*, 2007).

A cross-Peninsula pressure gradient (e.g. of ∼1.5 hPa across the gap upwind of Whirlwind Inlet at a height of 1500 m at 1000 UTC on 5 February; not illustrated) and jet trajectory descent above the lee slopes (Figures 11 and 12(d–f)) indicates that the gap flow acceleration is a result of both gap flow forcing (the cross-AP pressure gradient and flow convergence) and mountain-wave-generated momentum flux. Moreover, although

not presented here (see instead Elvidge *et al.* (2014)), there is clear evidence of mountain-wave breaking – a phenomenon commonly associated with strongly accelerated downslope winds (Durran, 1990) – across both the gaps and the higher sections of the AP.

Figures 11 and 12 confirm that the air is potentially cooler and moister towards the sea surface upwind of the AP, and hence that the source air for the jet regions is on average cooler and moister than that for the wake regions (i.e. wake trajectories are associated with greater isentropic drawdown). The greatest jet–wake discrepancy in $\theta$ ($q$) at the 150 km upwind distance increment is ∼6.3 K (∼1.1 g kg$^{-1}$) for the CI and S of CI regions (Figure 12). Note that the largest difference in upwind trajectory source altitude is also for this jet–wake pair. The other two jet–wake pairs exhibit $\theta$ ($q$) differences of between 2 and 2.5 K (between 0.25 and 0.29 g kg$^{-1}$) at the 150 km upwind distance increment.

The sourcing of near-surface leeside air from significantly higher altitudes upwind is diagnostic of upwind flow blocking, which is predicted by the relatively large value of $\hat{h}$ (3.4) representative of this event (Sheppard, 1956; Smith, 1989). Flow is more effectively blocked by the higher orography upwind of the wakes.

Note in discussion of Figure 8 (in section 5.1), conditions within the wake region to the south of MOI were highlighted as anomalous, with similar temperatures to and higher humidities than the air making up the MOI jet. Back trajectory analysis (not shown) explains this anomaly by showing that air within this wake was derived from low altitudes (a mean of ∼550 m AMSL at a distance 150 km upwind of the AP's crest) within Marguerite Bay, yet was not strongly accelerated to form a jet. The reason for this is unclear, though is presumed to be a consequence of the complex terrain and/or mesoscale pressure gradients.

### 6.2. *Cases B and C*

An identical Lagrangian analysis (not shown) of case B reveals similar results to case A, confirming that the foehn jets in this case are also gap flows, sourced from lower, cooler and moister regions upwind of the AP. The foehn air is generally sourced from lower altitudes than in case A (indicative of a shallower layer of blocked flow). As its analysis does not contribute significantly to understanding beyond that provided by analysis of cases A and C, case B is not further discussed here.

In case C the generally much stronger winds (Figure 2(c)) and large variability in wind speeds close to the Peninsula means using a wind speed criterion which does not distinguish the jets and wakes cleanly, and introduces bias in the distance downwind of the lee slopes for the sample areas. Instead temperature is used to distinguish the jets and wakes, making the assumption that foehn jets are characterised by relatively cool temperatures (as illustrated in Figure 9(a,b), and in cases A and B). Jets and wakes are defined by temperatures at the height (950 hPa) and time of trajectory initiation under 278 K and over 280 K respectively. It should be noted that a wind speed criterion was also tested, and was found to produce qualitatively similar sampling regions and trajectory results as those produced using the temperature criterion. Note that due to the northwest orientation of the approaching flow (Table 1) there is no MOI jet in this case, so only the WI, CI and adjacent wake regions are considered (marked in Figure 13).

Figures 13 and 14 show case C trajectories initiated within the WI jet in horizontal and vertical space respectively. Cross-Peninsula flow is shown to be from the northwest, with little deviation in flow direction across the AP. As previously the trajectories have a relatively common source region (Figure 13), and wake trajectories pass above the AP's crest at, on average, higher elevations (Figure 14).* In contrast to case A, the low-level

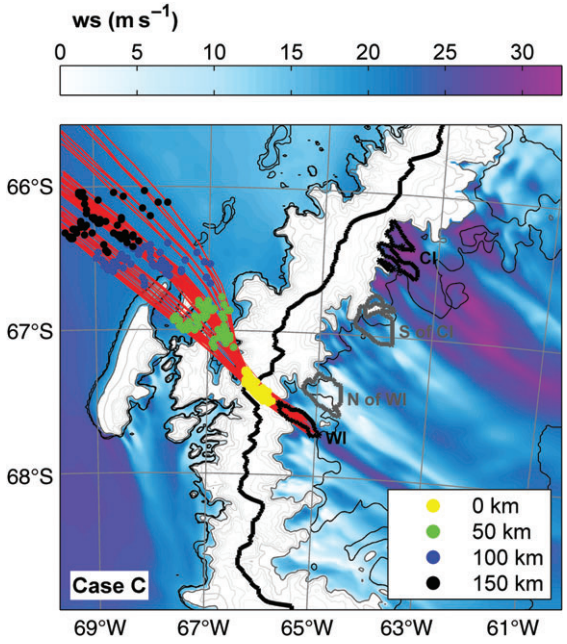


**Figure 13.** Back trajectories overlying wind speed, as in Figure 10(a), but showing case C WI jet trajectories at 2200 UTC 15 November 2010. To enhance legibility only half the trajectories are plotted.

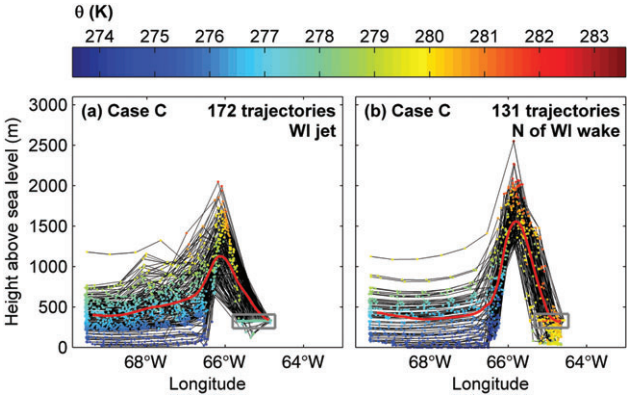


**Figure 14.** Back trajectories vs. longitude, as in Figure 11(a) but for case C trajectories initiated at 2200 UTC 15 November 2010 within (a) the WI jet and (b) the N of WI wake. In (a) all and in (b) half the trajectories are plotted.

foehn air is, for both WI and N of WI regions, derived from similarly low levels upwind. Despite this, a clear low-level cross-Peninsula temperature gradient is apparent, especially in the case of the N of WI wake region (Figure 14(b)). Vertical fluctuations in some WI trajectories upwind of the AP are due to the disturbance of the flow by the northern tip of Adelaide Island.

Figure 15 presents a summary of case C trajectory results. For the N of WI wake region some trajectories are 'lost' (∼28%) between the 0 and 50 km increments of distance upwind of the AP (Figure 15(a)) due to 'intersection' with orography – an unphysical occurrence that is a consequence of the limitations of the NWP model and the time step used to calculate the trajectories (3 min). Despite this, enough trajectories remain (typically hundreds) to provide statistically robust results. For the CI jet region virtually all trajectories are lost at the 100 km point (and none remain at 150 km) due to leaving the domain to the north (Figure 15(b)). For the same reason S of CI wake region

*Note that, counterintuitively, the peak orographic heights traversed – indicated by the horizontal lines in Figure 15(c,d) – are in all cases above the mean height of the corresponding trajectories above the AP. This quirk is due to the 30 min trajectory model output interval, and the fact that trajectories are deemed to be above the AP at the first model output for which they pass the crest (hence these heights are underestimates – more so in case C than in case A due to greater wind speeds meaning greater advective distances during the 30 min interval), whereas peak orographic height is calculated by interpolating between locations of trajectories either side of the crest.

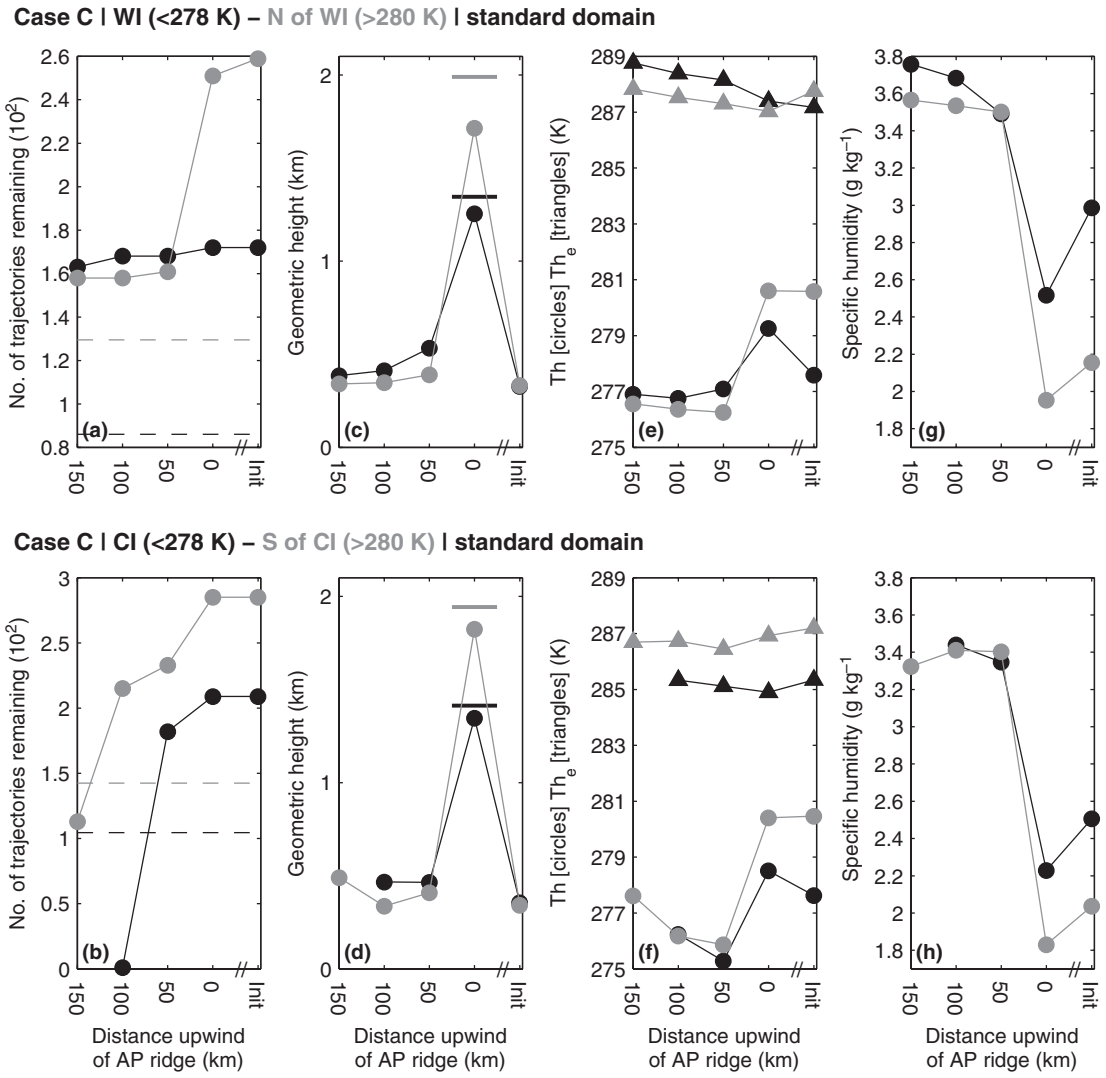


**Figure 15.** Lagrangian changes for mean back trajectories, as in Figure 12, but for back trajectories initiated at 2200 UTC on 15 November 2010 during case C. Diagnostics illustrated are (a, b) number of trajectories; (c, d) geometric height; (e, f) $\theta$ (Th; circular markers) and equivalent $\theta$ (The; triangular markers); and (g, h) $q$.

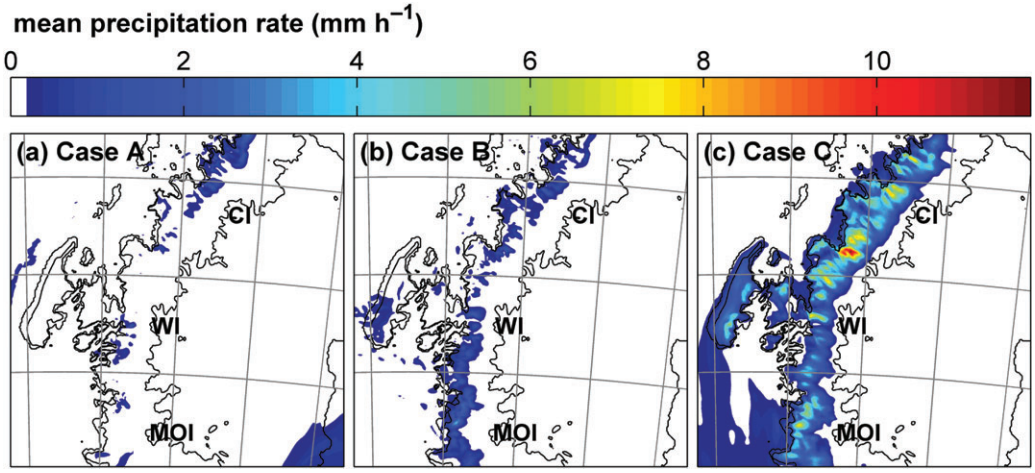


**Figure 16.** Mean precipitation rate for the 12 h after (a) 2200 UTC on 4 February 2011 during case A, (b) 1200 UTC on 27 January during case B, and (c) 1000 UTC 15 November 2010 during case C, according to the MetUM 1.5 km simulation.

trajectories are gradually lost with upwind distance, though most (75%) still remain at the 100 km upwind distance increment.

In case C there is little difference in mean trajectory height between trajectory initiation and 100 km upwind of the AP in any of the regions (Figure 15(c,d)). This is in agreement with the small value of $\hat{h}$ associated with this foehn event (representative $\hat{h} = 0.9$). Note that, according to Ólafsson and Bougeault (1996), for three-dimensional, non-rotating, hydrostatic flow with constant wind and stability over an elongated ridge (whose long edge is perpendicular to the flow), $\hat{h} < 1.2$ implies $z_d = 0$, i.e. no flow blocking. Moreover, this critical value of $\hat{h}$ is an underestimate since it ignores the effect of rotation, which in this case (given the high latitude) is significant, and has been found to encourage flow-over (Ólafsson and Bougeault, 1997). The relatively low upwind source altitude for the foehn suggests that the contribution of isentropic drawdown to warming in the

lee of the AP will be small. The fact that the foehn effect is still apparent (there is a clear cross-Peninsula temperature and moisture gradient; Figures 9(b,c) and 14) is a result of diabatic heating and moisture loss which occurs as air rises and crosses the AP. Latent heating is apparent from Figure 15 in the convergence of $\theta$ and $\theta_e$ – associated with the decrease in $q$ – along trajectories across the AP. In case C the decreases in $q$ are substantial, between 0.77 and 1.41 g kg$^{-1}$, considerably more than seen in case A. During case C thick cloud cover is simulated upwind (not shown), together with much greater rates of precipitation above the windward slopes of the AP (Figure 16). This can be explained by greater background humidities (compare Figures 12(j–l) and 15(g,h)) and greater expansion cooling associated with the greater ascent of air above the windward slopes. Sensible heating is also apparent for two of the four case C regions in the Lagrangian increase in $\theta_e$ across the AP due to mechanical mixing, though this warming is small relative to that caused by latent heating due to precipitation (Figure 15(e,f)). Note that the contribution of direct radiative heating to $\Delta\theta_e$ is neglected as insignificant (in accordance with MetUM 1.5 km $\theta$ budget analysis not shown here).

In common with cases A and B the jet trajectories for case C cross the Peninsula at lower altitudes than the wake trajectories (on average), confirming again that these are *gap flows*. However, as described in section 5.2, the foehn jets of case C are less distinct and peak winds are at higher levels. Indeed, case C exhibits the characteristics of *deep foehn* (e.g. Mayr *et al.*, 2007), with gap jets apparent though embedded within strong cross-Peninsula flow above (to heights exceeding the maximum height of the Figure 9(d) cross-section and above the AP's orography – not shown), contrasting with the distinct *shallow gaps flows* of case A (Figure 8(d)).

In case C, jet air is sourced from approximately the same heights upwind of the AP as wake air (reflected in similar upwind $\theta$ and $q$), a result consistent with the flow regime being linear for all sections of the ridge ($\hat{h} < 1.2$, independent of whether $h$ is chosen as the mean peak height traversed by the jet or by the wake trajectories). Whereas in cases A and B differences in the source altitude of the foehn were largely responsible for the cool, moist nature of the jets relative to the wakes, in case C differences in diabatic heat exchanges are the cause. Along the wake trajectories $q$ drops by a far greater amount across the AP due to a comparatively large loss of moisture (predominantly in the form of precipitation; Figure 16) as the trajectories rise over the AP's windward slopes (between 50 and 0 km upwind of the AP's crest; Figure 15(g,h)). The greater precipitation is associated with the greater upwind ascent required for air to surmount the higher sections of the AP's crest, and results in greater net irreversible latent heat release, warming the air as it rises. This is reflected in the convergence of $\theta$ and $\theta_e$ lines for the wake trajectories being greater than for the jet trajectories (Figure 15(e,f)).

### 6.3. Summary

The trajectory analysis for the nonlinear case A has demonstrated that near-surface leeside air is sourced from higher altitudes upwind and that the jet and wake regions have distinct sources of upwind air; the jets generally have lower altitude (thus cooler and moister) source regions than the wakes. For the more linear case C, near-surface leeside foehn air is sourced from near-surface levels upwind (i.e. there is little isentropic drawdown) and there is little difference in the source altitudes for the jets and wakes. In case C it is differences in the amount of upwind ascent which explains their cool, moist signature. The greater ascent required for flow to traverse the higher sections of the AP ridge results in greater orographic precipitation (resulting in latent heat gain and moisture loss) for the ascending air upwind of the wake regions than the jet regions. Case B, characterised by weaker (stronger) flow blocking and marginally greater (much weaker) precipitation rates than in case A (C), appears to reside somewhere in between the two cases in regards to linearity and warming mechanisms.

## 7. Synthesis and conclusions

During three differing cases of westerly foehn above the LCIS, foehn air was able to penetrate to near-surface levels, mixing and flushing away any residual cool air which typically pools above the Larsen Ice Shelf. The MetUM 1.5 km simulations were found to provide reasonably accurate representations of the foehn events when compared with the aircraft observations, giving us confidence that these simulations could be used to help understand the dynamics of the events. A back trajectory model forced by MetUM 1.5 km data provided insight into the source of foehn air and the evolution of flow as it passed the AP.

In case A a highly nonlinear cross-Peninsula flow regime evolved, associated with low-level upwind flow blocking causing the leeside air to be derived from relatively high elevations upwind. As such the drawdown of air from aloft appears to be the major driver of foehn warming and drying. The warming contributions made by the various foehn mechanisms towards all three cases presented here will be quantified in a future piece of work. The most significant warming was found at the base of the lee slopes where the advective warming and turbulent mixing induced by the foehn dominates over cooling to the ice surface (this is discussed further in Elvidge *et al.* (2014)).

In case C strong northwesterly and comparatively weakly stratified flow led to a relatively linear flow regime. Little upwind flow blocking was apparent, with foehn trajectories derived from low levels to the west of the AP. In this case large precipitation rates associated with irreversible latent heating are largely responsible for the warming and drying. The precipitation is triggered by the ascent from low level of moist maritime air above the windward slopes.

During all three foehn cases, the near-surface flow field immediately to the lee of the AP consists of jets emanating from the mouths of inlets, separated by regions of calmer flow (referred to as 'wakes' here). These jets above the LCIS are a new discovery: such features of foehn flow in the polar regions have not previously been investigated, nor seen so clearly in other foehn-prone regions. They are on the order of 10–60 km in width close to the base of the lee slopes, dispersing with distance downwind though persisting for a great distance (hundreds of km, i.e. across the entirety of the LCIS). They have been revealed via trajectory analysis to be the downwind continuation of gap flows across passes in the AP's ridge. The approximate position and strength of one of these jets – the Whirlwind Inlet jet – has been verified by aircraft observations from both cases A and B. This jet was found to extend to near-surface level and be characterised by gusty westerly winds reaching speeds in excess of 20 m s$^{-1}$.

In case A the foehn jets are distinct and confined to low levels above the LCIS. Outside of the jets the leeside foehn flow is weak in comparison. Such *shallow gap flows* reflect the nonlinearity of the flow regime. The jets are a product of both gap flow (the cross-AP pressure gradient and flow convergence within the gaps) and mountain-wave forcing mechanisms.

In case C the foehn jets are stronger (reaching speeds in excess of 30 m s$^{-1}$) and less distinct from the surrounding foehn flow, which is far stronger than in case A. The leeside flow field is altogether more homogenous in both the horizontal and vertical dimensions than in case A, resembling cases of *deep foehn* in the Alps. Reduced gap flow acceleration and stronger, deeper foehn flow extending downwind of all sections of the AP to greater distances downwind (in the absence of a strong hydraulic jump) is consistent with the strong cross-AP flow and the linear nature of the flow regime (Gaberšek and Durran, 2004).

Near-surface conditions within the jets, whilst warmer and drier than upwind and further east above the LCIS, are in all three cases moister and cooler than those of the adjacent wake regions,

typically by 3–4 K and 0.5–1.2 g kg$^{-1}$. This is due to a dampened foehn effect as a result of flow upwind of the jets passing over lower terrain. During the nonlinear case A the jet air is sourced from lower, potentially cooler and moister regions. During the linear case C, there is reduced latent heating and drying (due to less precipitation) upwind and above the mountain passes than over the peaks.

The jets studied here are qualitatively similar to foehn-driven gap-flow accelerated jets elsewhere in the world, though they are notable because of their distinct temperature and moisture signature and leeside extent. Their existence has important implications for the Larsen Ice Shelf. Their impact on the ice is evident in the occurrence of large sastrugi within WI during case A. Kuipers Munneke *et al.* (2012) used automatic weather station observations during the same foehn event as case C to show that foehn conditions can bring about particularly high melt rates on the Larsen C. A recent study making use of satellite synthetic aperture radar backscatter data has found that the distribution of annual surface melt duration on the Larsen C corresponds closely to that which may be expected as a result of foehn warming (Luckman *et al.*, 2014), i.e. the satellite-derived melt patterns closely match the foehn warming evident during case A with greatest warming at the foot of the lee slopes (Figure 8(b)). Moreover, the highest melt regions were found to be within the major inlets north of MOI, notably WI and CI, within which foehn jets have been observed, implying these foehn jets are playing a significant role in ice melt. Although the jet air is cooler than the wake air, foehn penetration to the surface would be expected to be more frequent within the inlets, due to the possibility of gap winds here even during weak, otherwise blocked cross-AP flow, or southerly to southwesterly roughly AP-parallel flow (where pressure gradients drive gap flows), e.g. in CI during case A (Figure 10(b)), and see Zängl (2002). Furthermore, the greater air–ice exchange of heat and moisture results in a more closely coupled air–surface interface, which – given warm enough foehn – would result in greater surface warming beneath the jets. Further investigation into the surface energy balance aspects of foehn flows on the LCIS is needed. Observations of surface fluxes both during and in the absence of foehn jets would be particularly helpful in assessing the impact of jets on ice melt. With this knowledge the impact of the recent, highly documented changing large-scale circulation around Antarctica on the ice shelves east of the AP may be better understood.

The AP is generally poorly represented in climate models due to its narrow, steep topography, thus orographic phenomena such as foehn flows and their associated warming will not be adequately modelled. Given the climatic implications of westerly foehn on the Larsen C Ice Shelf, the findings of this study and other recent studies (Kuipers Munneke *et al.*, 2012; Elvidge *et al.*, 2014; Luckman *et al.*, 2014) underline the need for the next generation of climate models to account for the foehn effect in some way, particularly with regard to low-level flow acceleration and regional warming.

## Acknowledgements

This article was made possible by funding provided by NERC under the project grant NE/G014124/1. All members of the OFCAP project, the Field Operations team and others at Rothera Research Station are acknowledged for valuable contributions towards the planning, technical and practical aspects of the observational data capture during the field campaign, and subsequent quality control and processing of data. We thank the NCAS team at the University of Reading, S. Webster and S. Vosper for advice and assistance with the running of the MetUM, and T. Phillips for providing the orography data. We acknowledge use of the MONSooN system, a collaborative facility supplied under the Joint Weather and Climate Research Programme, which is a strategic partnership between the Met Office and the Natural Environment Research Council. A. Ross and A. Matthews provided useful discussion and comments during the first author's PhD Viva. Technical assistance with the running of Lagranto was provided by M. Sprenger.

## Supporting information

The following supporting information is available as part of the online article:

**Appendix S1.** Model validation for upwind conditions using aircraft observations.

**Table S1.** A comparison of aircraft and model variables from upwind profiles.

## References

Beran DW. 1967. Large amplitude lee waves and chinook winds. *J. Appl. Meteorol.* **6**: 865–877.

Bolton D. 1980. The computation of equivalent potential temperature. *Mon. Weather Rev.* **108**: 1046–1053.

Brinkmann WA. 1974. Strong downslope winds at Boulder, Colorado. *Mon. Weather Rev.* **102**: 592–602.

van den Broeke M. 2005. Strong surface melting preceded collapse of Antarctic Peninsula ice shelf. *Geophys. Res. Lett.* **32**: L12815, doi: 10.1029/2005GL023247.

Brown AR, Beare RJ, Edwards JM, Lock AP, Keogh SJ, Milton SF, Walters DN. 2008. Upgrades to the boundary-layer scheme in the Met Office numerical weather prediction model. *Boundary-Layer Meteorol.* **128**: 117–132.

Colle BA, Mass CF. 1998. Windstorms along the western side of the Washington Cascade Mountains. Part I: A high-resolution observational and modeling study of the 12 February 1995 event. *Mon. Weather Rev.* **126**: 28–52.

Davies T, Cullen MJP, Malcolm AJ, Mawson MH, Staniforth A, White AA, Wood N. 2005. A new dynamical core for the Met Office's global and regional modelling of the atmosphere. *Q. J. R. Meteorol. Soc.* **131**: 1759–1782.

Dee DP, Uppala SM, Simmons AJ, Berrisford P, Poli P, Kobayashi S, Andrae U, Balmaseda MA, Balsamo G, Bauer P, Bechtold P, Beljaars ACM, van de Berg L, Bidlot J, Bormann N, Delsol C, Dragani R, Fuentes M, Geer AJ, Haimberger L, Healy SB, Hersbach H, Hólm EV, Isaksen L, Kållberg P, Köhler M, Matricardi M, McNally AP, Monge-Sanz BM, Morcrette J-J, Park B-K, Peubey C, de Rosnay P, Tavolato C, Thépaut J-N, Vitart F. 2011. The ERA-Interim reanalysis: Configuration and performance of the data assimilation system. *Q. J. R. Meteorol. Soc.* **137**: 553–597.

Durran DR. 1986. Another look at downslope windstorms. Part I: The development of analogs to supercritical flow in an infinitely deep, continuously stratified fluid. *J. Atmos. Sci.* **43**: 2527–2543.

Durran DR. 1990. Mountain waves and downslope winds. In *Atmospheric Processes over Complex Terrain*, Blumen W. (ed.) *Meteorological Monographs* 23: 59–81. American Meteorological Society: Boston, MA.

Elvidge AD, Renfrew IA, King JC, Orr A, Lachlan-Cope TA. 2014. Foehn warming distributions in nonlinear and linear flow regimes: A focus on the Antarctic Peninsula. *Q. J. R. Meteorol. Soc* (in press).

Fiedler EK, Lachlan-Cope TA, Renfrew IA, King JC. 2010. Convective heat transfer over thin ice covered coastal polynyas. *J. Geophys. Res.* **115**: C10051, doi: 10.1029/2009JC005797.

Flamant C, Drobinski P, Nance L, Banta R, Darby L, Dusek J, Hardesty M, Pelon J, Richard E. 2002. Gap flow in an Alpine valley during a shallow south foehn event: Observations, numerical simulations and hydraulic analogue. *Q. J. R. Meteorol. Soc.* **128**: 1173–1210.

Gaberšek S, Durran DR. 2004. Gap flows through idealized topography. Part I: Forcing by large-scale winds in the nonrotating limit. *J. Atmos. Sci.* **61**: 2846–2862.

Garman KE, Hill KA, Wyss P, Carlsen M, Zimmerman JR, Stirm BH, Carney TQ, Santini R, Shepson PB. 2006. An airborne and wind tunnel evaluation of a wind turbulence measurement system for aircraft-based flux measurements. *J. Atmos. Oceanic Technol.* **23**: 1696–1708.

Hunt JCR, Snyder WH. 1980. Experiments on stably and neutrally stratified flow over a model three-dimensional hill. *J. Fluid Mech.* **96**: 671–704.

King JC, Lachlan-Cope TA, Ladkin RS, Weiss A. 2008. Airborne measurements in the stable boundary layer over the Larsen Ice Shelf, Antarctica. *Boundary-Layer Meteorol.* **127**: 413–428.

Kuipers Munneke P, van den Broeke MR, King JC, Gray T, Reijmer CH. 2012. Near-surface climate and surface energy budget of Larsen C ice shelf, Antarctic Peninsula. *The Cryosphere* **6**: 353–363.

van Lipzig NPM, Marshall GJ, Orr A, King JC. 2008. The relationship between the Southern Hemisphere Annular Mode and Antarctic Peninsula summer temperatures: Analysis of a high-resolution model climatology. *J. Climate* **21**: 1649–1668.

Liu H, Jezek KC, Li B, Zhao Z. 2001. *RADARSAT Antarctic Mapping Project Digital Elevation Model.* National Snow and Ice Data Center. Digital Media. National Snow and Ice Data Centre: Boulder, CO.

Luckman A, Elvidge AD, Jansen D, Kulessa B, Kuipers Munneke P, King JC, Berrand NE. 2014. Surface melt and ponding on Larsen C Ice Shelf and the impact of foehn winds. *Antarct. Sci.* (in press).

Marshall GJ. 2002. Trends in Antarctic geopotential height and temperature: A comparison between radiosonde and NCEP-NCAR reanalysis data. *J. Clim.* **15**: 659–674.

Marshall GJ, Orr A, van Lipzig NP, King JC. 2006. The impact of a changing Southern Hemisphere Annular Mode on Antarctic Peninsula summer temperatures. *J. Clim.* **19**: 5388–5404.

Mayr GJ, Armi L, Gohm A, Zängl G, Durran DR, Flamant C, Gaberšek S, Mobbs S, Ross A, Weissmann M. 2007. Gap flows: Results from the Mesoscale Alpine Programme. *Q. J. R. Meteorol. Soc.* **133**: 881–896.

Morris EM, Vaughan DG. 2003. Spatial and temporal variation of surface temperature on the Antarctic Peninsula and the limit of viability of ice shelves. In *Antarctic Peninsula Climate Variability: Historical and Paleoenvironmental Perspectives*, Domack E, Leventer A, Burnett A, Bindschadler R, Convey P, Kirby M. (eds.) *Antarctic Research Series* 79: 61–68. AGU: Washington, DC.

Ólafsson H. 2005. The heat source of the foehn. *Hrvatski Meteorološki Časopis* **40**: 542–545.

Ólafsson H, Bougeault P. 1996. Nonlinear flow past an elliptic mountain ridge. *J. Atmos. Sci.* **53**: 2465–2489.

Ólafsson H, Bougeault P. 1997. The effect of rotation and surface friction on orographic drag. *J. Atmos. Sci.* **54**: 193–210.

Orr A, Marshall GJ, Hunt JC, Sommeria J, Wang CG, van Lipzig NP, Cresswell D, King JC. 2008. Characteristics of summer airflow over the Antarctic Peninsula in response to recent strengthening of westerly circumpolar winds. *J. Atmos. Sci.* **65**: 1396–1413.

Orr A, Phillips T, Webster S, Elvidge AD, Weeks M, Hosking JS, Turner J. 2014. Met Office Unified Model high-resolution simulations of a strong wind event in Antarctica. *Q. J. R. Meteorol. Soc.*, doi: 10.1002/qj.2296.

Overland JE, Walter BA Jr. 1981. Gap winds in the Strait of Juan de Fuca. *Mon. Weather Rev.* **109**: 2221–2233.

Pan F, Smith RB. 1999. Gap winds and wakes: SAR observations and numerical simulations. *J. Atmos. Sci.* **56**: 905–923.

Rignot E, Casassa G, Gogineni P, Krabill W, Rivera A, Thomas R. 2004. Accelerated ice discharge from the Antarctic Peninsula following the collapse of Larsen B Ice Shelf. *Geophys. Res. Lett.* **31**: L18401, doi: 10.1029/2004GL020697.

Rignot E, Box JE, Burgess E, Hanna E. 2008. Mass balance of the Greenland ice sheet from 1958 to 2007. *Geophys. Res. Lett.* **35**: L20502, doi: 10.1029/2008GL035417.

Scambos TA, Hulbe C, Fahnestock M, Bohlander J. 2000. The link between climate warming and break-up of ice shelves in the Antarctic Peninsula. *J. Glaciol.* **46**: 516–530.

Sheppard PA. 1956. Airflow over mountains. *Q. J. R. Meteorol. Soc.* **82**: 528–529.

Smith RB. 1979. The influence of mountains on the atmosphere. *Adv. Geophys.* **21**: 87–230.

Smith RB. 1980. Linear theory of stratified hydrostatic flow past an isolated mountain. *Tellus* **32**: 348–364.

Smith RB. 1989. Mountain-induced stagnation points in hydrostatic flow. *Tellus A* **41**: 270–274.

Stark JD, Donlon CJ, Martin MJ, McCulloch ME. 2007. 'OSTIA: An operational, high resolution, real time, global sea surface temperature analysis system.' *Proceedings of Oceans '07 IEEE Conference, 'Marine Challenges: Coastline to Deep Sea'*, 18–21 June 2007, Aberdeen, UK.

Trombetti F, Tampieri F. 1987. An application of the dividing-streamline concept to the stable airflow over mesoscale mountains. *Mon. Weather Rev.* **115**: 1802–1806.

Vaughan DG, Doake CSM. 1996. Recent atmospheric warming and retreat of ice shelves on the Antarctic Peninsula. *Nature* **379**: 328–331.

Vaughan DG, Marshall GJ, Connolley WM, King JC, Mulvaney R. 2001. Devil in the detail. *Science* **293**: 1777–1779.

Vaughan DG, Marshall GJ, Connolley WM, Parkinson C, Mulvaney R, Hodgson DA, King JC, Pudsey CJ, Turner J. 2003. Recent rapid regional climate warming on the Antarctic Peninsula. *Clim. Change* **60**: 243–274.

Webster S, Uddstrom M, Oliver H, Vosper S. 2008. A high-resolution modelling case study of a severe weather event over New Zealand. *Atmos. Sci. Lett.* **9**: 119–128.

Wernli BH, Davies HC. 1997. A Lagrangian-based analysis of extratropical cyclones. I: The method and some applications. *Q. J. R. Meteorol. Soc.* **123**: 467–489.

Whiteman CD. 2000. *Mountain Meteorology: Fundamentals and applications.* Pacific Northwest National Laboratory. Oxford University Press: New York, NY.

WMO. 1992. *International Meteorological Vocabulary* (2nd edn), WMO-No. 182. World Meteorological Organization: Geneva, Switzerland.

Zängl G. 2002. Idealized numerical simulations of shallow foehn. *Q. J. R. Meteorol. Soc.* **128**: 431–450.

Zängl G. 2003. Deep and shallow south foehn in the region of Innsbruck: Typical features and semi-idealized numerical simulations. *Meteorol. Atmos. Phys.* **83**: 237–261.

Zängl G, Chimani B, Häberli C. 2004. Numerical simulations of the foehn in the Rhine Valley on 24 October 1999 (MAP IOP 10). *Mon. Weather Rev.* **132**: 368–389.